



Structural characteristics and optical properties of plasma assisted reactive magnetron sputtered dielectric thin films for planar waveguiding applications

S.J. Pearce ^{a,*}, M.D.B. Charlton ^a, J. Hiltunen ^b, J. Puustinen ^c, J. Lappalainen ^c, J.S. Wilkinson ^d

^a Electronic and Computer Science, University of Southampton, SO17 1BJ, United Kingdom

^b VTT, Oulu, FIN-90571, Finland

^c Microelectronics and Materials Physics Laboratories, University of Oulu, FIN-900014, Finland

^d Optoelectronics Research Center, University of Southampton, SO17 1BJ, United Kingdom

ARTICLE INFO

Article history:

Received 15 February 2012

Accepted in revised form 26 May 2012

Available online 5 June 2012

Keywords:

Dielectrics

Crystalline

Amorphous

Reactive sputtering

Feedback control

Thin film deposition

ABSTRACT

Thin films of aluminum oxide (Al_2O_3), tantalum pentoxide (Ta_2O_5), titanium oxide (TiO_2), yttrium oxide (Y_2O_3) and zirconium oxide (ZrO_2) were deposited by plasma assisted reactive dual magnetron sputtering to determine their suitability as a host for a rare earth doped planar waveguide upconversion laser. The effect of deposition parameters such as cathode, plasma power and oxygen gas flows were studied and the operational working points were determined. Both power and lambda control were used to optimize the optical quality of each material. By using lambda control feedback system, the magnetron power fluctuates to sustain a fixed oxygen flow in the target area reducing the compound layer growth on the material and maintaining a healthy deposition rate. The optical properties, structure and crystalline phase of each film were found to be dependent on the process parameters. X-ray diffraction (XRD) analysis revealed that the thin films varied from amorphous to highly crystalline depending on the deposition conditions. X-ray photoelectron spectroscopy (XPS) was utilized for surface compositional analysis revealing that films had varying stoichiometric ratios which are controlled for each material by the deposition parameters chosen. The waveguide loss for the thin film layers was investigated and Ta_2O_5 was shown to have a slab waveguide loss of ~ 1 dB/cm at both visible and infra-red wavelengths making it ideal for planar waveguide and laser applications. TiO_2 , Y_2O_3 and ZrO_2 were found to deposit in a highly crystalline phase. Waveguiding in the TiO_2 layers was not possible at 633 nm or in the infrared region. The Y_2O_3 samples gave low loss (2–4 dB/cm) at the 1.3 and 1.5 μm wavelengths but no waveguiding at 633 nm or 833 nm was possible. Atomic force microscopy showed rough surface topography for TiO_2 , Y_2O_3 and ZrO_2 akin to their crystalline growth with the SEM images confirming the regular crystalline columnar structure for the case of Y_2O_3 and ZrO_2 .

© 2012 Elsevier B.V. Open access under CC BY license.

1. Introduction

There has been considerable interest in optimization of the deposition processes for planar waveguide materials as hosts for solid-state lasers and optical amplifiers. These include aluminum oxide [1], zirconium oxide [2], titanium oxide [3], scandium oxide [4], yttrium oxide [5–7] and tantalum pentoxide [8]. Planar waveguide lasers based on rare earth doped thin films provide a desirable method to achieve high optical gain in a small and compact device [5]. Essential properties of host materials include: low optical loss, low peak phonon energy, ability to be doped and ability to waveguide at the pump and emission wavelengths.

Aluminum oxide (Al_2O_3) when deposited as a thin film has a moderate refractive index (1.6–1.7) [9–12] and has a wide transmittance range from 200 nm up to 7 μm . Al_2O_3 thin films have good adhesion, hardness,

durability and anti-wear properties. These characteristics make it an ideal material for many applications such as optical interference coatings, multilayer polarizers and filters and micro-electromechanical systems (MEMS). Another key application for Al_2O_3 thin films is insulating layers in metal–oxide–semiconductor (MOS) transistors. Methods to deposit Al_2O_3 include plasma enhanced chemical vapor deposition [13], dual ion beam sputtering [14], plasma assisted electron beam evaporation [15,16], plasma assisted reactive magnetron sputtering [17], direct current reactive magnetron sputtering [10], pulsed laser deposition (PLD) [18] and cathodic arc deposition [19]. Aluminum oxide has already been proven as a suitable host material for rare earth dopants [20,21]. In particular erbium doped optical waveguide amplifiers operating at 1.53 μm with a net optical gain of 2.3 dB have been reported [22]. Very low optical loss (1 dB/cm) Al_2O_3 ridge waveguides have previously been created by post annealing films at 800 °C [23].

Due to its high dielectric constant, high refractive index in the visible spectral range [24] and high chemical and thermal stability, tantalum pentoxide (Ta_2O_5) thin films have been studied for applications such as high density dynamic random access memories (DRAMs) [25,26],

* Corresponding author. Tel.: +44 2380593127.

E-mail address: sp3@ecs.soton.ac.uk (S.J. Pearce).

decoupling capacitors [27,28], antireflection coatings [29,30] and optical waveguides [31]. Many different techniques to deposit Ta_2O_5 thin films have been utilized allowing its use in compact photonic circuits and as a potential host for rare earth ions to achieve optical gain [32]. Ta_2O_5 has a large energy band gap of 4.2 eV [24] which in principle allows nearly absorption free transmission from 400 nm to 10 μm

[33], and is a proven host material for rare earth dopants [32,33], with low phonon energy and capability to produce low loss waveguides [34].

Titanium oxide (TiO_2) is an important material for optical applications such as antireflective coatings [35], microelectronic devices [36,37] and protective layers [38], has a high refractive index and is transparent across the visible wavelength range. The waveguiding

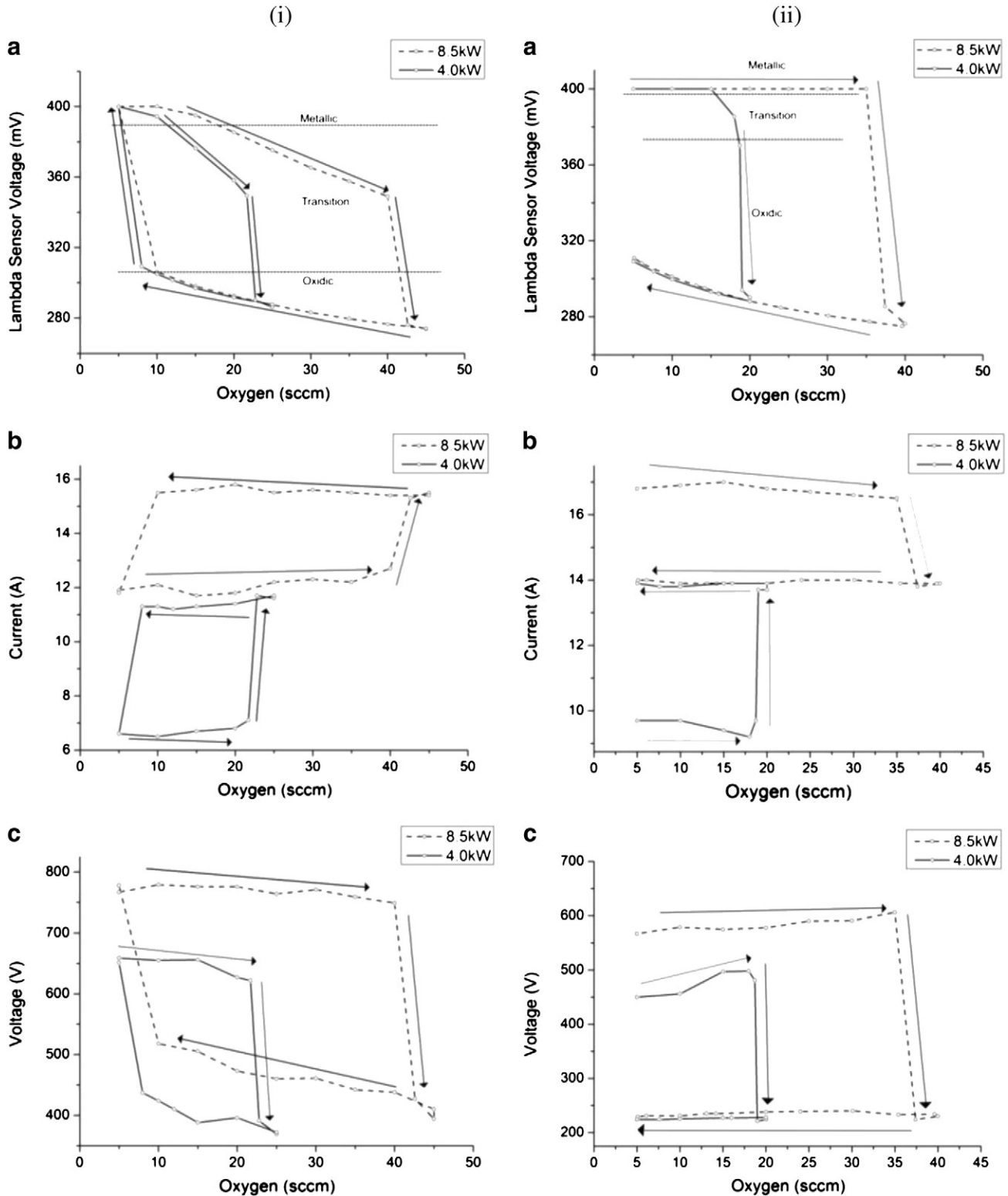


Fig. 1. Comparison of operational curves for (i) Al_2O_3 and (ii) Y_2O_3 measured at two target power levels, 8.5 kW and 4.0 kW. Argon flow in the target area: 35 sccm. The additional plasma source was operated at 1.5 kW with an oxygen flow rate of 15 sccm. The lambda sensor voltage behavior is shown in (a), cathode target current in (b) and cathode target voltage in (c).

properties of TiO₂ made by magnetron sputtering [39], PLD [40] and sol gel methods [41] have been studied. The TiO₂ deposited by these methods is often in the crystalline phase inducing scattering losses. TiO₂ exhibits three distinct crystalline forms apart from amorphous, rutile (tetragonal), anatase (tetragonal) and brookite (orthorhombic). When deposited at temperatures below ~80 °C an amorphous layer is produced, further increases in temperature up to ~350 °C will deposit the anatase phase, and the rutile phase dominates at temperatures over 350 °C [42]. The generation of the anatase and rutile phases depends strongly on the deposition method and temperature. Each crystalline phase has different applications. The rutile phase is mainly used in optical applications such as high refractive index prisms. The anatase form has many interesting properties, which make it a promising material for applications such as photocatalysis, gas sensors, dielectrics in memory cell capacitors and semiconductor field effect transistors [43].

Among the available host materials, the dielectric yttrium oxide (Y₂O₃) has received much attention in recent years due to its suitability as a waveguide and a laser host [44]. Its desirable material properties include high refractive index (1.7–1.9) [45–47], large band gap, excellent thermal conductivity, low dominant phonon energy [48,49], broad transparency range and easy doping with rare earth ions such as erbium [6]. Both Y₂O₃ and erbium oxide have a cubic crystal structure with very similar lattice constants and trivalent yttrium and erbium have nearly the same ionic radius [5,50] making doping easier due to very little lattice mismatch between the two materials. One disadvantage of Y₂O₃ is its tendency to crystallize which can lead to high waveguide losses especially in the visible region [51]. However, the crystallized structure can be advantageous to other applications such as high *k* gate dielectric layers [52]. Previous work on Y₂O₃ [53] showed that the deposition method used determines the structure and optical quality of the layer with amorphous layers being deposited using Y₂O₃ material in an oxygen rich atmosphere in an electron beam evaporator.

Zirconium oxide (ZrO₂) is extensively used as a coating in a wide range of applications due to its many desirable properties such as high refractive index (2.1 at 550 nm), broad spectral region of low absorption from 240 nm to 8 μm, low resistance against oxidation, excellent thermal stability and high laser damage threshold. Thin films deposited by electron beam evaporation [54], reactive sputtering [55,56], ion-assisted deposition [57], and PLD [58] have previously been reported. Similar to TiO₂, the structure and properties of the deposited film are influenced by the deposition conditions, such as pressure, oxygen partial pressure, substrate temperature and RF power. ZrO₂ appears in a variety of crystalline phases, at low temperatures, and monoclinic phases exist with indices of 2.1–2.2 in its bulk form.

At a higher temperature the crystalline structure changes to cubic [59]. The structural and optical properties of sol–gel derived erbium doped zirconium oxide thin films for waveguide applications have been studied [60] and ion beam assisted sputtered erbium doped zirconium oxide has been used in optical amplification [2] giving low loss and gain at 1534 nm. Atomic layer deposited crystalline erbium doped zirconium oxide has more recently been used in improving capacitor properties [61].

Reactive sputtering is a technique to deposit high quality metal oxide or nitride thin films by sputtering metallic targets in the presence of a reactive gas mixed with an inert gas (usually argon). The structure of the deposited film depends largely on the deposition parameters such as sputtering rate, the distance between the target and substrate, substrate temperature and the partial pressures of the reactive and inert gasses. The sputtering process has three distinct modes of operation – metallic, transient and oxidic. The transition between the metallic and oxidic modes occurs abruptly at two different values of the reactive gas flow depending on the direction of the reactive gas partial pressure. In the metallic mode, the film is mainly metallic and the target is free of any oxides. It gives higher rates of deposition (>1.5 nm/s for Ta) and due to the metallic nature of the layer, very high absorption is standard. In the transient mode, the number of reactions continuously increases with more oxygen (dependent on target material) and metal atoms combining to form the oxide. As the thin film becomes more transparent deposition rates (<0.6 nm/s for Ta₂O₅) and optical absorption are much lower. During the oxidic mode, nearly all the metal atoms are oxidized, the deposited thin films are transparent with a surplus of oxygen in the target area not consumed by the chemical process. Further increases to the oxygen flow “poison” the metal target creating an insulating film on the surface. This thin insulating film on the surface of the metal target leads to much lower sputtering rates. By reducing the reactive gas in the target area the flow can no longer maintain the insulating layer and the target returns to the metallic mode giving higher deposition rates and higher absorption. This behavior (which follows a hysteresis curve) is typical for reactive sputtering processes. For the optimum thin film layers the sputtering process must be stable without any target poisoning. The optical (refractive index, waveguide loss, etc.) and structural (crystal structure, atomic composition, uniformity etc.) properties of the oxide layer are directly determined by flow of oxygen in the target area, the deposition power and the substrate temperature.

The aim of the present study is to report on the structural and optical properties of Al₂O₃, Ta₂O₅, TiO₂, Y₂O₃ and ZrO₂. A unique feedback sensor was used to create a stable deposition condition within the target area improving the quality of the thin film coatings. In addition,

Table 1
Reactive sputtering process parameters for each metal target. The argon flow rate in the cathode target was kept constant at 35 sccm and the additional plasma source was constant at 1.5 kW power and 15 sccm oxygen.

Material	Al ₂ O ₃			Ta ₂ O ₅		TiO ₂		Y ₂ O ₃		ZrO ₂		
Sample no.	(i)	(ii)	(iii)	(i)	(ii)	(i)	(ii)	(i)	(ii)	(i)	(ii)	(iii)
Cathode O ₂ (sccm)	30	20	10	72.5	37	20	10	16.4	6.3	53	27.6	12.2
Cathode power (kW)	8.5	4.1	2.6	8.5	4	4	2	4	2	8.5	4	2
Lambda voltage (mV)		340		306	315	379.4		384	381.9		345	
Thickness (nm)	556	352	564	732	770	480	509	664	715	525	614	720
Deposition rate (nm/s)	0.371	0.234	0.128	0.732	0.385	0.480	0.255	0.332	0.179	0.525	0.307	0.18
Roughness RMS (nm)	0.199	0.211	0.239	0.179	0.186	7.49	7.40	0.375	0.643	0.878	0.982	1.96
Refractive index												
500 nm	1.671	1.658	1.656	2.230	2.238	2.680	2.674	1.959	1.958	2.246	2.242	2.262
800 nm	1.658	1.646	1.643	2.162	2.171	2.505	2.493	1.930	1.928	2.204	2.195	2.212
1000 nm	1.655	1.644	1.641	2.150	2.159	2.479	2.466	1.923	1.921	2.196	2.185	2.202
Waveguide loss (dB/cm)												
633 nm	35	50	26	1	1	–	–	–	–	–	–	–
833 nm	15	10	6	1	1	–	–	–	–	–	–	19
1320 nm	10	10	5	1	1	–	–	2	3	–	18	10
1552 nm	10	10	4	1	1	–	–	2	4	–	11	5
Atomic ratio	1.81	1.80	1.77	3.17	3.27	2.04	2.06	2.15	2.47	3.14	2.77	2.74

the deposition parameters for each material were optimized using a standard hysteresis curve associated with reactive sputtering. The optimized thin films were characterized using a wide range of tools to determine their suitability for planar waveguide applications i.e. as a host material for an upconversion laser.

2. Waveguide preparation

Films were deposited on an unheated <100> orientated silicon substrates with a thermally grown 2 μm thick SiO_2 layer. The SiO_2 layer enabled a slab waveguide to be created for the purpose of optical transmission measurements. Prior to deposition, the substrates were cleaned using a low intensity oxygen plasma using an additional RF plasma source. This additional step improves adhesion and removes any surface contamination. The deposition of high quality metal oxide layers was achieved by plasma assisted reactive magnetron sputtering (PARMS) in a Leybold Optics Helios Pro XL system. This process combines reactive middle frequency sputtering with partial pressure control, and a reactive assist process with an additional RF plasma source. This two step process gives highly oxidized films with good uniformity and controllable stoichiometry. During each rotation of the plate holding the substrate, a thin sub-stoichiometric oxide was deposited by the dual magnetron metal target. The layer is then transformed to a non-absorbing oxide layer by passing under the oxygen plasma of the RF source. To ensure high layer thickness precision the Helios system uses an optical monitoring system (OMS5000) to accurately calculate the thickness of the layer being deposited in real time. As the thickness of the coating increases, the intensity of the reflected light periodically changes at the surface of the optical coating in a predictable manner. The OMS response is constantly compared to a layer by layer transfer-matrix based simulation. During the deposition process for each material, the voltage on the lambda sensor (the sensor which detects oxygen in the chamber) and the magnetron target voltage and current were monitored with respect to the oxygen flow rate into the target area. The unusual lambda control system gives a better quality of deposited film than the simple power control (as used in most other systems) as the deposition conditions are actively adjusted to maintain a constant gas environment in the target/magnetron area. It is well known that reactive sputtering is highly unstable, with the magnetron target quickly switching from a metallic state into a poisoned state. By using a feedback system (lambda control), the magnetron power fluctuates to sustain a fixed oxygen flow in the target area reducing the compound layer growth on the material and maintaining a healthy deposition rate. The feedback system consists of two electrodes around a ZrO_2 element, which operates at a temperature of 700 $^\circ\text{C}$. One electrode is located within the ZrO_2 tube and exposed to the atmosphere, while the other is on the surface of the ZrO_2 tube exposed to vacuum. The output voltage of the sensor is proportional to the logarithm of the oxygen partial pressure difference at the electrodes.

For each material the chamber was evacuated using turbo pumps to a base pressure of 8×10^{-7} mbar. Each magnetron target consisted of two 12" by 4" 99.9% purity metal targets. The substrates sit on a large platen located ~10 cm below the target/magnetron set which rotates at 180 RPM. High purity argon and oxygen were introduced into the target area through specially designed injectors. Oxygen was introduced separately into the additional plasma source operating at a fixed power of 1.5 kW to further oxidize the layers. The flow rates of both gasses were separately controlled through mass flow controllers. Fig. 1 shows a comparison between (a) the lambda sensor voltage, (b) the cathode current and (c) the cathode voltage with respect to an increasing oxygen flow rate (sccm, standard cubic centimeters per minute) into the target area at two cathode power levels 4 kW and 8.5 kW for two materials only (i) Al_2O_3 and (ii) Y_2O_3 . By monitoring the process a suitable lambda voltage could be chosen to control the reactive sputtering process. This allowed a lambda sensor working point to be determined for a given oxygen flow within the transition

mode optimizing the stability of the deposition process, the deposition rate and the thin film properties required. The modes of operation have been marked on the image as a guide.

As the oxygen flow rate increases the lambda sensor voltage decreases. When a certain flow rate is reached the target poisons and the lambda sensor voltage drop to its minimum (~280 mV). For the aluminum target the cathode voltage initially remains stable with increasing oxygen flow until it reaches a peak value, corresponding to the poisoning of the target. The voltage then decreases with further increases in the oxygen flow rate. With decreasing oxygen flow rate, the cathode voltage stabilizes until a point is reached where the plasma clears the oxide layer on the surface of the target and returns to the metallic mode. The cathode current follows the same operational curve as the voltage but increases at the point at which the target is poisoned. It is interesting to note that when operating at 8.5 kW the cathode current for the yttrium target is initially at a high value and decreases as the target is poisoned. The operational curves for the

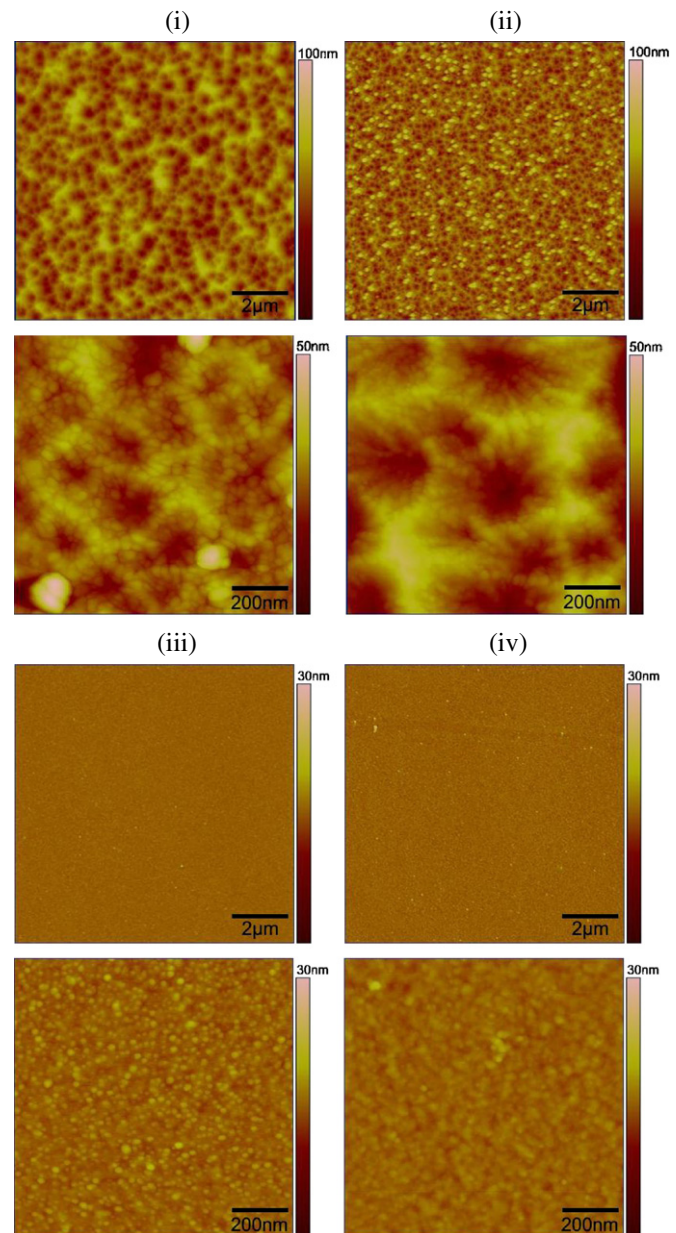


Fig. 2. Atomic force microscope images for each deposited sample of (i) TiO_2 sample (i), TiO_2 sample (ii), (iii) Y_2O_3 sample (i) and (iv) Y_2O_3 sample (ii).

yttrium target show that the target failed to recover to the initial starting value and remained poisoned. The compound layer grown on the surface of the target during the oxidic region of the hysteresis curve remains intact until the oxygen flow is reduced to 0 sccm. With the oxygen removed, the plasma is able to clean the thin compound layer from the surface and returns the target to its metallic state. It is also of interest to note that at 8.5 kW there is no working point for the yttrium target. The lambda sensor voltage rapidly decreases from 400 mV to 284 mV without a gradual slope as seen with the aluminum metal target. Choosing a suitable lambda control voltage and producing high quality optical layers were difficult at this higher power level. The target either operated in the metallic mode of operation depositing layers with high absorption or was continuously poisoned in the oxidic mode and ceased operation with little or no deposition of Y_2O_3 . The yttrium target was therefore operated at a fixed cathode plasma power of 4 kW and 2 kW and a constant oxygen flow without using the lambda control sensor. In addition, due to their ease of oxidation and subsequent poisoning, the zirconium, aluminum and titanium targets were also operated at 2 kW and reduced oxygen flow rate for comparison with the latter operated on a fixed oxygen flow. Using the operational curves for each material, an oxygen flow rate and subsequently a lambda control voltage were chosen. As mentioned previously, lambda control is used to maintain a constant oxygen concentration in the sputter chamber by varying the cathode plasma power allowing for a stable deposition process.

Table 1 shows the deposition parameters used for each deposition. For titanium, yttrium and zirconium, lambda control was not used but the sensor voltage was recorded. To maintain the lambda voltage within the transition area of the operational curves for these materials, the oxygen flow rate was altered for each cathode power used. Furthermore, the titanium and yttrium targets failed to deposit a transparent oxide layer when operated at 8.5 kW regardless of the amount of oxygen flow rate used.

The optical and structural properties of the deposited films were characterized using X-ray diffraction (XRD) using a conventional θ – 2θ arrangement with Cu K α radiation from a Philips PW1380 operating at a voltage and current of 40 kV and 40 mA, respectively, X-ray photoelectron spectroscopy (XPS) using a commercial theta probe instrument (Thermo Fisher Scientific) with parallel detection capability to acquire surveys and element specific high-resolution spectra of each deposited sample, scanning electron microscopy (SEM) using a JEOL 7500 field emission scanning electron microscope (FESEM), atomic

force microscopy (AFM) measured using a Veeco Dimension 3100 atomic force microscope in a tapping mode, waveguide loss for each material measured using a Metricon 2010 prism coupling system at four wavelengths ranging from the visible to the infra-red and variable-angle spectroscopic ellipsometry (VASE).

3. Characterization results and discussions

Variable-angle spectroscopic ellipsometry (VASE) was used to determine the refractive index at various wavelengths in the visible and near infrared of the as-deposited thin films. Table 1 shows the dependence of the refractive indices at three different wavelengths of the incident light for the Al_2O_3 , Ta_2O_5 , TiO_2 , Y_2O_3 and ZrO_2 thin films respectively. The refractive index shows a slight dependency on the plasma power indicating an improved film density of the layers deposited at higher plasma powers. The refractive index for each material showed similarities to other thin film works [23,24,35,45,56]. An amorphous layer will have a lower refractive index than a crystalline layer due to the difference in densities between them. This could be attributed to a uniform inclusion of nanometer scale air voids [62]. Furthermore at high pressures the low species kinetic energy for certain sputtered ions prevents crystalline growth and leads to an amorphous film [63]. Thin films produced under these conditions can exhibit lower refractive indices than the bulk [6,45].

Fig. 2 shows the topographic views of the TiO_2 and Y_2O_3 thin films and Fig. 3 shows the surface of the ZrO_2 thin films. The root-mean-square roughness values can be seen in Table 1. It can be seen that for the majority of the materials deposited the surface roughness varies inversely with the magnetron power. This behavior was attributed to an increase of the grain size for the deposited layer [64,65]. The surfaces for Ta_2O_5 and Al_2O_3 are not shown here as they were clear and smooth which is analogous with the amorphous layers showing no interesting structures whereas for films of a crystalline nature i.e. TiO_2 , Y_2O_3 and ZrO_2 the surface appears rougher. For the rougher samples a further measurement at 1 μm was made to show the large features on the surface. The TiO_2 films show surface features of ~ 40 nm in size with craters forming over the surface, and Y_2O_3 and ZrO_2 samples have features of ~ 15 – 35 nm with rms roughness (R_q) values of around 7.5, 0.5 and 1.0 nm, respectively, as shown also in Table 1. The growth of certain physical vapor deposition (PVD) materials can be described using a structure zone model [66]. The growth morphology depends on the gas pressure and substrate temperatures, at low gas pressures

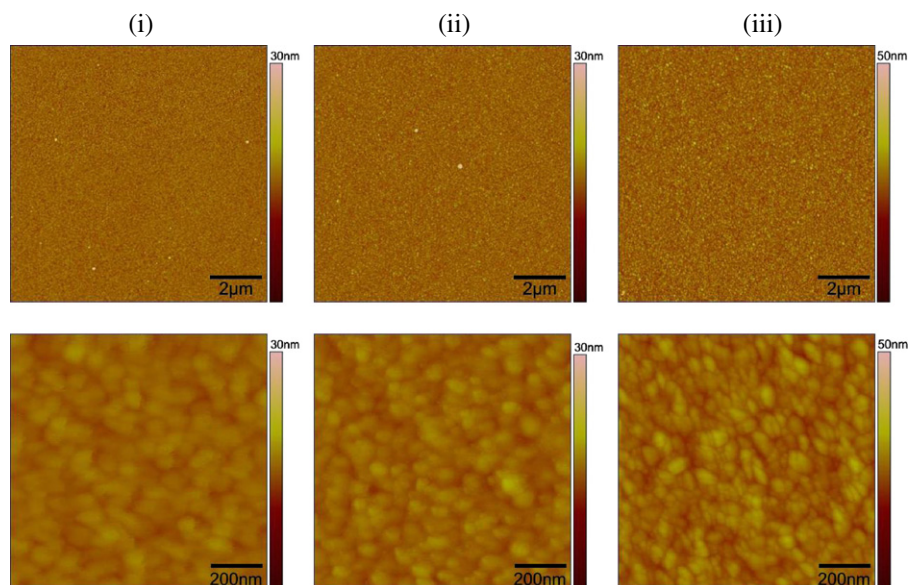


Fig. 3. Atomic force microscope images for each deposited sample of (i) ZrO_2 sample (i), ZrO_2 sample (ii), and (iii) ZrO_2 sample (iii).

and substrate temperatures the film will consist of a dense and smooth structure. At high pressure and low substrate temperature, columnar micro crystalline growth with voids is formed. As the substrate temperature rises, the grain size will increase, increasing the surface roughness. When TiO_2 films are deposited under high pressure a more porous microstructure with a rough surface is obtained. In addition with a low ion bombardment the films will grow open grain boundaries and large columns. The void fraction in the material is increased due to a decrease in the island density and an increase in the average grain size [67].

Fig. 4 shows the cross sectional SEM images for sample 1 for each material. As can be seen the Ta_2O_5 and Al_2O_3 layers are smooth indicating amorphous growth as suggested by the AFM studies. The Y_2O_3 and ZrO_2 images show a columnar structure analogous to its crystalline growth. It is interesting to note that the first ~ 200 nm of TiO_2 deposited has what seems to be an amorphous structure and then continues with a rough crystalline structure. This was attributed to the temperature increase in the chamber during the latter part of the deposition (due to plasma heating effects). At low substrate temperatures, amorphous

TiO_2 is frequently observed [68] to be attributed to the low energy and low mobility of particles impinging on the relatively cold surface of the substrate [69]. Polycrystalline materials can be defined as having an average grain size of approximately $1\ \mu\text{m}$ and may extend to several hundreds of microns. Amorphous materials lack the long range atomic order of a crystalline structure and appear smooth when imaged.

One of the important characteristics of any waveguiding layer is its propagation loss. Losses in thin waveguide layers originate from many factors [70], which include absorption in the core, leakage between the core and cladding and scattering losses. One of the key contributors to the scattering loss is the sizeable grain boundaries between neighboring crystal domains, which lead to a strong Rayleigh scattering of confined light out of the waveguide. The intensity of the scattered light is proportional to the Rayleigh scattering cross section which scales as $\lambda^{-4} \times R^{-2}$, (where R is the radius of the scattering particle). Hence by optimizing the deposition parameters, an amorphous layer, with no sizeable grain boundaries and small grain size can be achieved, minimizing the scattered light and as such reducing the waveguide loss.

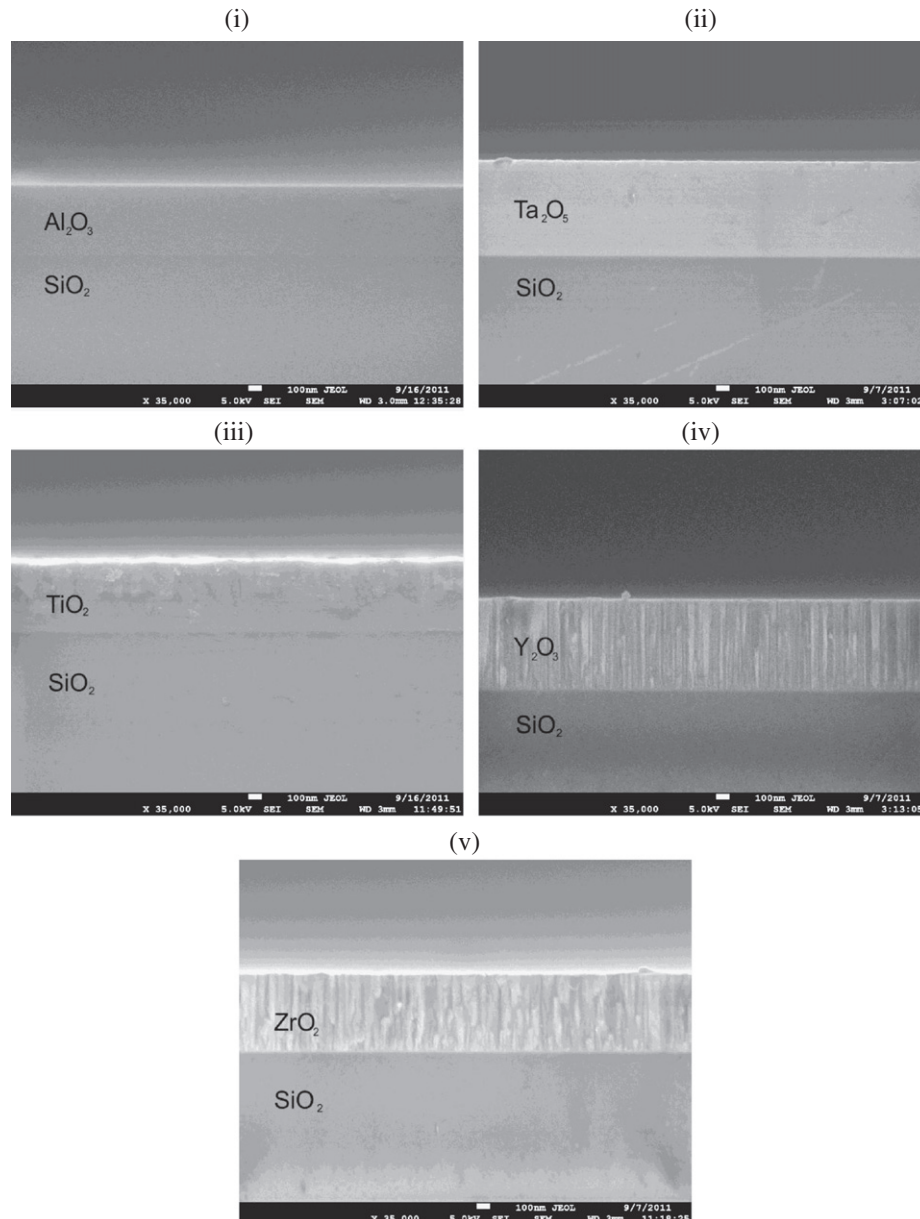


Fig. 4. SEM images of sample (i) for (i) Al_2O_3 , (ii) Ta_2O_5 , (iii) TiO_2 , (iv) Y_2O_3 and (v) ZrO_2 .

The light was coupled in slab waveguides using a prism and the intensity as a function of propagation distance was measured by scanning a detector coupled fiber. The minimum measurable loss value with the used setup was about 1 dB/cm. Table 1 shows the results of the waveguide loss measurements for each material deposited. The result shows that the waveguide loss is proportional to the cathode power suggesting that at lower deposition rates a higher optical quality of coating is possible. As is evident from the results the Ta₂O₅ layers gave the lowest waveguide loss, ideal for planar waveguide applications whereas no waveguiding was possible in the TiO₂ attributed to its highly crystalline nature, leading to large grain size and boundaries. The deposited Al₂O₃ shows a much larger waveguide loss than the Ta₂O₅ layers even though both materials grow as amorphous layers. This was attributed to voids within the deposited Al₂O₃ film and incomplete oxidation of the Al bonds, resulting in higher losses at lower wavelengths [71]. By depositing at an elevated temperature or post annealing the waveguide losses can be reduced [23,71,72]. Guiding was only possible in the infra-red wavelength range for the Y₂O₃ and ZrO₂ samples with high losses for the latter attributed to its growth structure and subsequently high scattering and absorption loss.

X-ray photoelectron spectroscopy (XPS) was used on the thin film layers deposited to determine their stoichiometric ratio. A microfocused monochromated Al K α X-ray source was set to illuminate a spot of 400 μ m in size using 50 eV pass energy and 0.1 eV step size for each element specific scan. During the XPS survey spectrum for each material the C 1s peak at a binding energy of 284.8 eV was observed. This was

attributed to the surface contamination after exposure to air and was used to verify charge compensation by the low energy electron flood gun. Fig. 5 (i) shows the element scans for each Al₂O₃ sample. Samples (i), (ii) and (iii) all show the Al 2p_{3/2} and O1s binding energies of ~74 eV and ~531 eV respectively corresponding to the Al₂O₃ form. Elemental analysis of the XPS data yields an O to Al ratio that is higher than the expected 1.5 indicating the presence of excess O on the surface of the thin films. Fig. 5 (ii) shows the element scans for both Ta₂O₅ samples. Both samples show peaks at ~26 eV (4f_{7/2}) and ~28 eV (4f_{5/2})

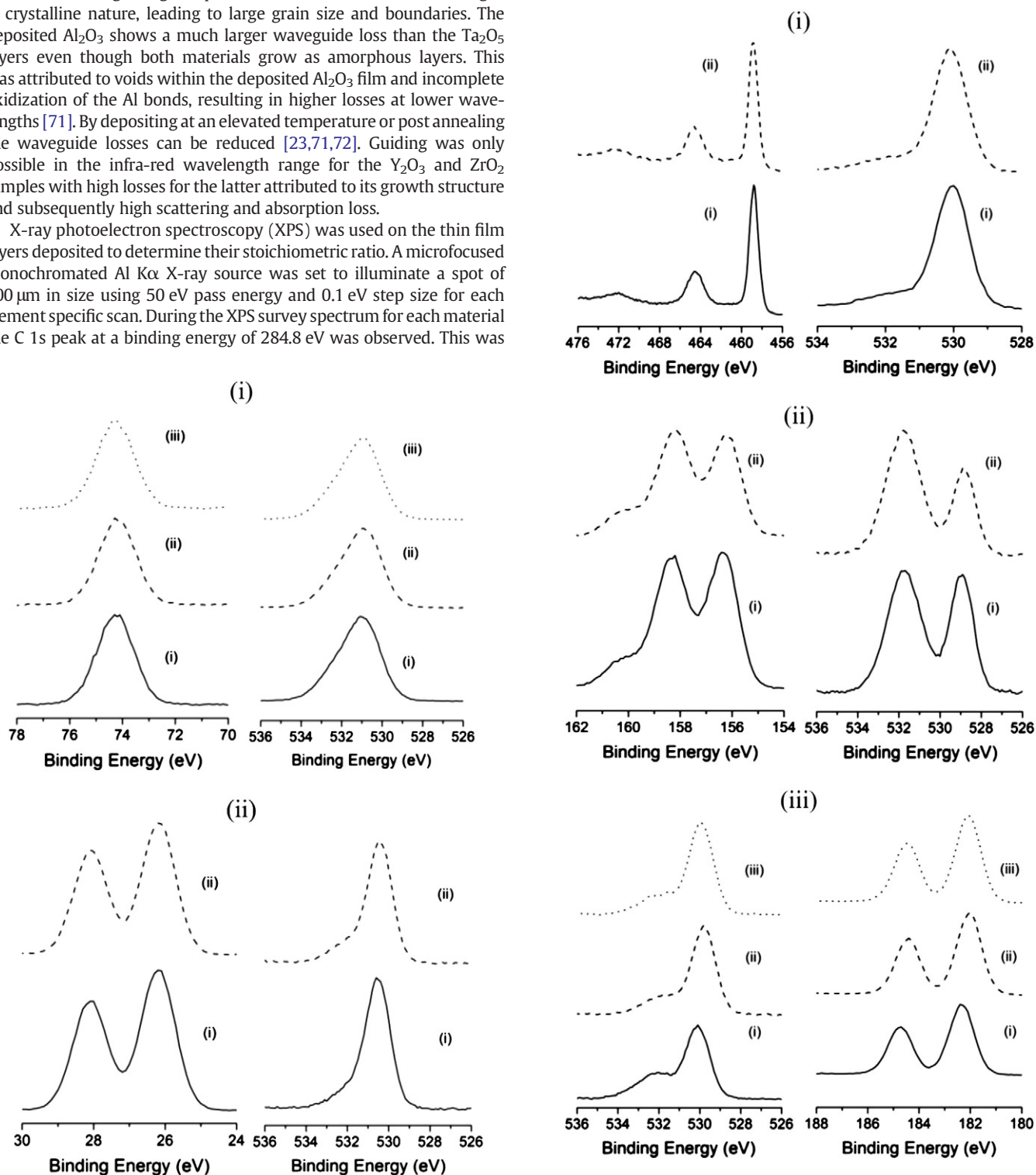


Fig. 5. X-ray photoelectron spectra for (i) Al₂O₃ (Al2p, O1s) and (ii) Ta₂O₅ (Ta4f, O1s).

Fig. 6. X-ray photoelectron spectra for (i) TiO₂ (Ti2p, O1s), (ii) Y₂O₃ (Y3d, O1s) and (iii) ZrO₂ (Zr3, O1s).

in a doublet corresponding to its oxide form. The atomic ratio for samples (i) and (ii) is shown in Table 1. Similar to the Al_2O_3 layers the O to Ta ratio was higher at the surface than the expected stoichiometric value of 2.5. This increase in atomic ratios for both metal oxides was attributed to a significant amount of oxygen containing species (hydroxide (OH) or carbonate (CO_3)) on the surface of the layers [73] increasing the oxygen content. The long tail seen on the O1s scan at the higher binding energies for both materials was attributed to a hydroxide (OH) contamination.

Fig. 6 (i) shows the elemental scan for the two TiO_2 samples. The $\text{Ti } 2p_{3/2}$ and $2p_{1/2}$ spin orbital splitting photoelectrons for each sample are located at the binding energies of ~ 458 eV and ~ 464 eV respectively. The position of the main peak, the separation between the $2p_{1/2}$ and $2p_{3/2}$ peaks of ~ 6 eV and the satellite at ~ 14 eV from the main peak are indicative of the TiO_2 layers. The shape of the TiO_2 O1s peak suggests that the surface has no carbonate or hydroxide species to increase the O. This is confirmed by elemental analysis of the XPS data which shows that the surface is stoichiometric compared to the other thin films deposited where the additional oxygen containing species increases the O to metal ratio.

Fig. 6 (ii) presents the elemental scan for each Y_2O_3 sample deposited. Two defined peaks are seen for both samples at ~ 156 eV and 158 eV corresponding to the spin orbit split between $3d_{3/2}$ and $3d_{5/2}$ of the yttria respectively [74,75]. The O1s scan shows strong peaks at ~ 529 eV and ~ 532 eV with a small shoulder peak at ~ 534 eV. The deposited Y_2O_3 films show two separate bonding doublets, one for pure Y_2O_3 (~ 156 eV and ~ 158 eV) and one attributed to the yttrium–hydroxide bonds (Y–OH) (~ 158 eV and ~ 160 eV). Yttrium containing films are known to react with ambient moisture when exposed to an atmosphere contaminating the surface of the film. Further investigations of the yttrium oxide surface was done using angle resolved XPS at 65° (top surface analysis) and 35° (below surface analysis). The results shown in Fig. 7 indicate that the contamination seen in the O1s, Y3d and C1s (not shown here) local scans is carbon and the doublet attributed to yttrium–hydroxide bonds is an yttrium–carbonate bond. The results show that at the surface of the thin film a high concentration of carbon is present but this is reduced as the depth into the thin film increases. This high concentration and the increase in O were attributed, as with the majority of the materials deposited, to the carbonate bonds on the surface of the thin film. The elemental scans for the three ZrO_2 samples are shown in Fig. 6 (iii). All three samples show a strong peak at ~ 182 eV ($3d_{5/2}$) and a small shoulder at ~ 184 eV ($3d_{3/2}$) which is associated with its oxide. Analysis of the XPS measurements shows that the O to Zr ratio for each sample (shown in Table 1) is close to ~ 3 which is attributed to the same conditions as suggested for the Al_2O_3 , Ta_2O_5 and Y_2O_3 thin films.

The structure and crystallinity of the deposited thin film layers were investigated by X-ray diffraction. θ – 2θ diffractograms were collected in the range of 10 – 60° although for the samples of Ta_2O_5 and Al_2O_3 the data was processed over the 10 – 35° range only. Fig. 8 (i–iv) shows the XRD patterns of the thin films deposited. The diffractograms for each Al_2O_3 and Ta_2O_5 sample (Fig. 8 (i)) confirm their amorphous growth regardless of the plasma power with only the Si peak at $\sim 33^\circ$ present. Slightly noisy intensity signals are partly averaged, as shown with the black lines, in order to express the amorphous background halos arising distinctively for the Al_2O_3 and Ta_2O_5 compounds with different oxygen ion concentrations and ionic radius of cations in the amorphous matrix. Fig. 8 (ii) shows the XRD patterns of the TiO_2 thin films investigated. As can be seen from the diffractograms, both TiO_2 samples have a small reflection peak at $\sim 26^\circ$ which can be attributed to its nanocrystalline anatase phase. An amorphous background is clearly seen also in the TiO_2 diffractograms for both deposition plasma powers, as pointed out for sample (ii) with a dashed line, indicating the existence of both crystalline and amorphous phases. This is actually seen also in Fig. 4 (iii) where it is obvious that the sample has two layers with a nanocrystalline TiO_2 layer on top of the amorphous TiO_2 bottom

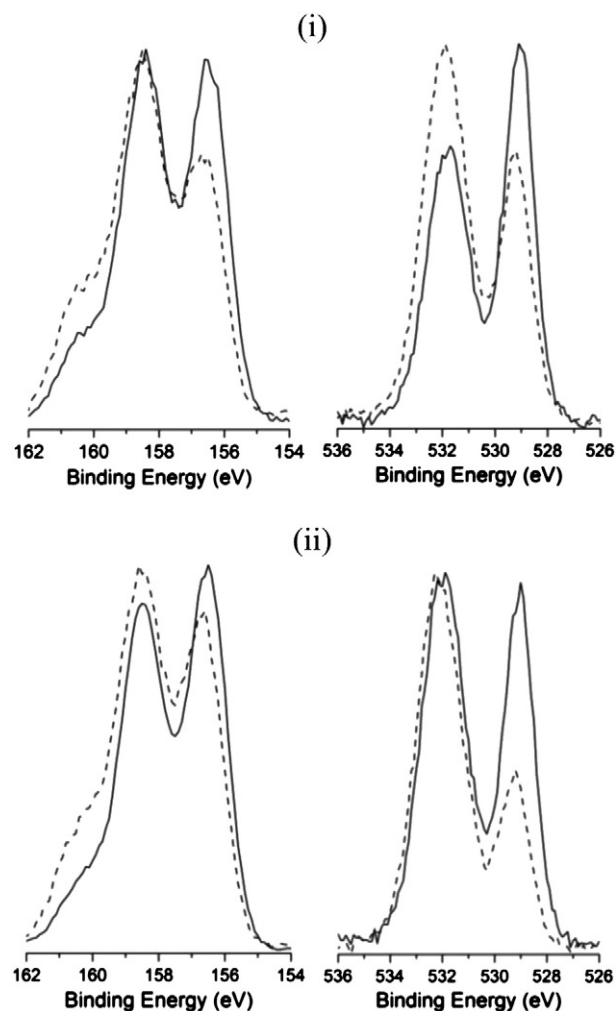


Fig. 7. Angular resolved X-ray photoelectron spectra for Y3d and O1s for sample (i) and sample (ii). Surface of the thin film (—) and below the surface (---).

layer. Fig. 8 (iii) shows the diffractograms for Y_2O_3 , each sample shows a peak at $\sim 29^\circ$ which corresponds to reflections from the $\langle 222 \rangle$ planes of Y_2O_3 [76]. The cubic phase of Y_2O_3 is expressed primarily by reflections from the $\langle 222 \rangle$ planes [44,77]. The high intensity of the reflection peak was attributed to the strongly aligned columnar structure of the cubic phase. Both samples show a weak diffraction peak at $\sim 40^\circ$ and $\sim 50^\circ$ which relates to reflections of the $\langle 332 \rangle$ and $\langle 440 \rangle$ planes suggesting that the films are cubic polycrystalline in nature [75,76]. Fig. 8 (iv) shows the XRD results for ZrO_2 . ZrO_2 has 4 different crystalline structures depending on the growth method and condition [78], these are monoclinic, tetragonal, cubic and amorphous. Based on the XRD results, the thin films deposited were of monoclinic and tetragonal phases but the more prominent peak at $\sim 28^\circ$ belongs to the monoclinic structure. However, the tetragonality of the minority phase increases with the decreasing oxygen content in the crystal structure from sample (i) to sample (iii). Like most thin film layers, the crystal structure changes as the temperature increases. At relatively low temperatures, amorphous structures are possible with small grain sizes whereas at elevated temperatures crystalline structures are more prevalent with much larger grain sizes.

4. Conclusions

Thin films of aluminum oxide, tantalum pentoxide, titanium oxide, yttrium oxide and zirconium oxide were deposited using a reactive middle-frequency dual magnetron sputtering system. The

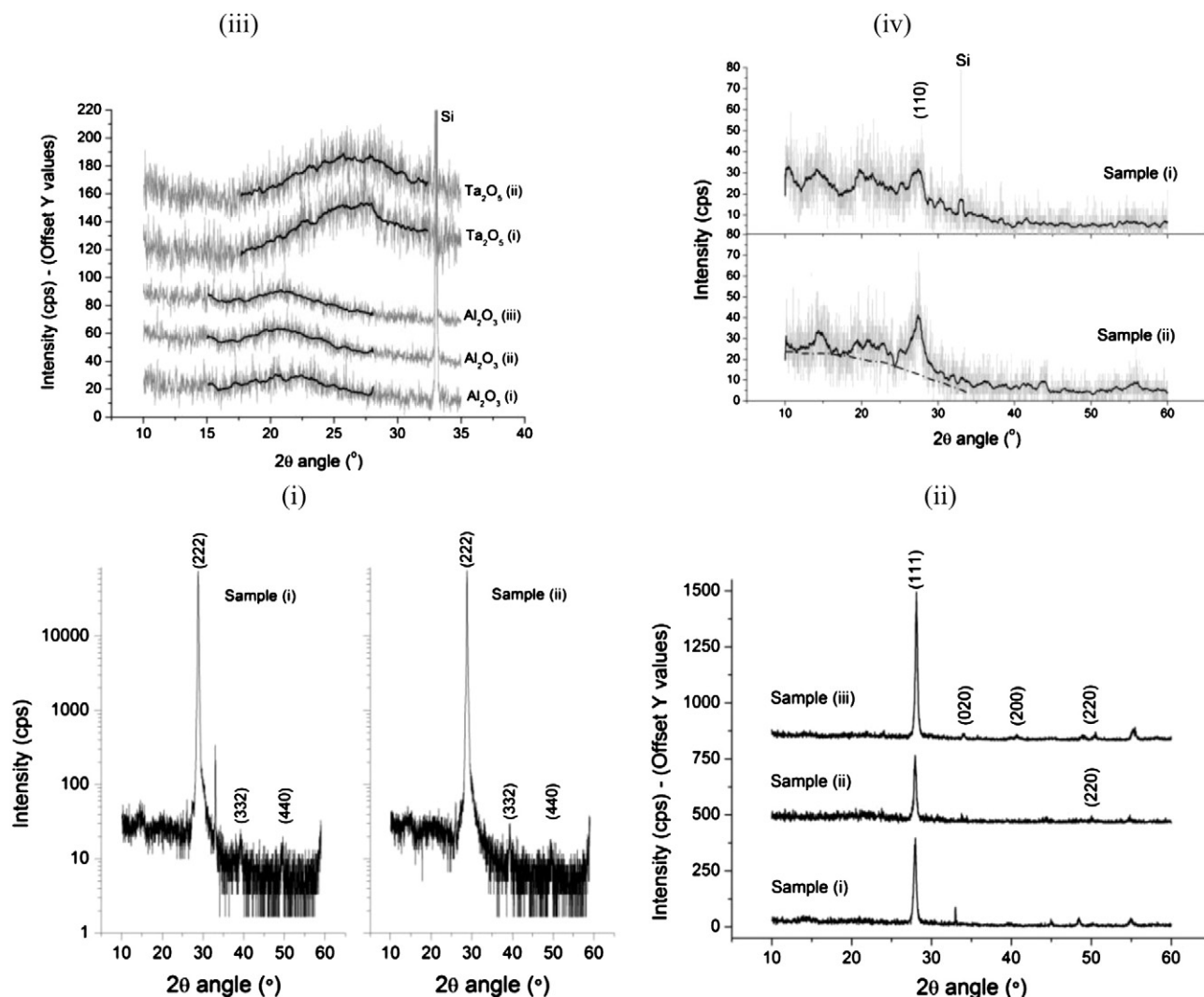


Fig. 8. XRD patterns for (i) Al_2O_3 and Ta_2O_5 , (ii) TiO_2 , (iii) Y_2O_3 and (iv) ZrO_2 thin films in the θ - 2θ mode.

operational parameters for each material in the form of hysteresis curves were investigated to determine a suitable lambda control voltage to maintain a fixed oxygen content in the target area. Thin films of each material were deposited at different plasma powers, oxygen flow rate and lambda control voltage to determine the best dielectric for use as a host for a rare earth dopant.

The films deposited were characterized using X-ray diffraction (XRD), X-ray photoelectron spectroscopy (XPS), scanning electron microscopy (SEM), atomic force microscopy (AFM), waveguide loss and variable-angle spectroscopic ellipsometry (VASE). The refractive index for each material agreed with other research data and showed that the deposition method and operational parameters used were correct.

The AFM image of the surface of the Al_2O_3 and Ta_2O_5 samples was smooth and analogous with the amorphous layers. This was confirmed by SEM which showed an amorphous structure with no distinguishable crystalline structure. However, for films of a crystalline nature i.e. TiO_2 , Y_2O_3 and ZrO_2 the surface appeared a lot rougher which was attributed to the larger grain size. The SEM images for these samples showed a regular columnar structure confirming the AFM results.

The guiding properties of each sample were examined in the infrared and visible regions. The results indicated that for the amorphous layers (Al_2O_3 and Ta_2O_5), guiding was possible from the visible to the infrared region of the spectrum making them both ideal candidates for a rare-earth doped upconversion waveguide laser. The TiO_2 films

failed to waveguide either in the visible or infrared wavelength range. This was attributed to its crystalline structure which increases the optical loss. However, the SEM images revealed that the TiO_2 layers were amorphous in growth until about 200 nm had been deposited and the layer changed to a crystalline structure. This was attributed to a temperature increase during the process due to the plasma at the target area and the additional oxidizing plasma used in the process run. The Y_2O_3 and ZrO_2 only showed guiding at 1320 nm and 1552 nm with low loss measured for the former at both wavelengths suggesting that the Y_2O_3 deposited could be doped with erbium for 1.5 μm applications.

X-ray photoelectron spectroscopy was used to analyze the composition of the samples at the surface. For all films deposited, except TiO_2 , the atomic ratio of oxygen to metal was higher than the expected stoichiometric values. This difference was attributed to two factors, firstly, XPS is a well known surface technique and cannot reveal the ratio for the bulk and secondly, the presence of additional oxygen containing species such as hydroxides and carbonates on the surface of the thin film increases its oxygen content.

The XRD results confirmed the amorphous nature of the Al_2O_3 and Ta_2O_5 samples and the crystalline growth of the TiO_2 , Y_2O_3 and ZrO_2 . The TiO_2 samples show that the structure of the layer changes as the temperature increases. At relatively low temperatures, amorphous TiO_2 is possible with small grain sizes whereas at elevated temperatures its crystalline phase is more prevalent with much larger grain sizes and higher optical losses.

Acknowledgments

The authors would like to thank Paul Mack from Thermo Fisher for the helpful and insightful XPS discussions. We express our gratitude to the EPSRC (grant number: EP/G003319/1) for funding this research. Jussi Hiltunen acknowledges the Academy of Finland for supporting his research under grant 133814.

References

- [1] C. Strohhofer, A. Polman, *Opt. Mater.* 21 (2003) 705.
- [2] R. Schermer, W. Berglund, C. Ford, R. Ramberg, A. Gopinath, *IEEE J. Quantum Electron.* 39 (2003) 154.
- [3] A. Bahtat, M. Bouderbala, M. Bahtat, M. Bouazaoui, J. Mugnier, M. Druetta, *Thin Solid Films* 323 (1998) 59.
- [4] Y. Kuzminykh, A. Kahn, G. Huber, *Opt. Mater.* 28 (2006) 883.
- [5] A. Peeva, A.Og. Dikovska, P. Atanasov, M. Jimenez de Castro, W. Skorupa, *Appl. Surf. Sci.* 253 (2007) 8165.
- [6] O. Pons, Y. Moll, A. Huignard, E. Antic-Fidancev, P. Aschehoug, B. Viana, E. Millon, J. Perriere, C. Garapon, J. Mugnier, *J. Lumin.* 87–89 (2000) 1115.
- [7] M. Korzenski, Ph. Lecoœur, B. Mercey, P. Camy, J. Doualan, *Appl. Phys. Lett.* 78 (2001) 1210.
- [8] C. Grivas, R.W. Eason, *J. Phys. Condens. Matter* 20 (2008) 264011.
- [9] M. Kharrazi Olsson, K. Macak, U. Helmersson, B. Hjorvarsson, *J. Vac. Sci. Technol., A* 16 (1998) 639.
- [10] W.D. Sproul, M.E. Graham, M.S. Wong, S. Lopez, D. Li, R.A. Scholl, *J. Vac. Sci. Technol., A* 13 (1995) 1188.
- [11] K.K. Shih, D.B. Dove, *J. Vac. Sci. Technol., A* 12 (1994) 321.
- [12] Z.W. Zhao, B.K. Tay, S.P. Lau, C.Y. Xiao, *J. Vac. Sci. Technol., A* 21 (2003) 906.
- [13] C.H. Lin, H.L. Wang, M.H. Hon, *Thin Solid Films* 283 (1996) 171.
- [14] G. Emiliani, S. Scaglione, *J. Vac. Sci. Technol., A* 5 (1987) 1824.
- [15] O. Stenzel, D. Gabler, S. Wilbrandt, N. Kaiser, H. Steffen, A. Ohl, *Opt. Mater.* 33 (2011) 1681.
- [16] J.B. Oliver, P. Kupinski, A.L. Rigatti, A.W. Schmid, J.C. Lambropoulos, S. Papernov, A. Kozlov, J. Spaulding, D. Sadowski, R. Chrzan, R.D. Hand, D.R. Gibson, I. Birnkley, F. Placido, *Appl. Opt.* 50 (2011) C19.
- [17] J.M. Andersson, E. Wallin, U. Helmersson, U. Kreissig, E.P. Munger, *Thin Solid Films* 513 (2006) 57.
- [18] A. Husmann, J. Gottmann, T. Klotzbucher, E.W. Kreutz, *Surf. Coat. Technol.* 100–101 (1998) 411.
- [19] S. Anders, A. Anders, M. Rubin, Z. Wang, S. Raoux, F. Kong, I.G. Brown, *Surf. Coat. Technol.* 1 (1995) 197.
- [20] X. Multone, Y. Luo, P. Hoffman, *Mater. Sci. Eng., B* 146 (2008) 35.
- [21] K. Solehmainen, M. Kapulainen, P. Heimala, K. Polamo, *IEEE Photon. Technol. Lett.* 16 (2004) 194.
- [22] G.N. van den Hoven, R.J.I.M. Koper, A. Polman, C. van Dam, J.W.M. van Uffelen, M.K. Smit, *Appl. Phys. Lett.* 68 (1996) 1886.
- [23] M.K. Smit, G.A. Acket, C.J. van der Laan, *Thin Solid Films* 138 (1986) 171.
- [24] C.Y. Huang, H.M. Ku, Y.P. Tsai, W.K. Chen, S. Chao, *Opt. Rev.* 16 (2009) 274.
- [25] K.A. McKinley, N.P. Sandler, *Thin Solid Films* 290 (1996) 440.
- [26] D. Spassov, E. Atanasova, D. Vironvska, *Appl. Phys. A* 82 (2006) 55.
- [27] S.-D. Cho, K.-W. Paik, *Mater. Sci. Eng., B* 67 (1999) 108.
- [28] L.W. Schaper, C. Thomason, *IEEE Trans. Compon. Packag. Technol.* 30 (2007) 563.
- [29] F. Rubio, J. Dennis, J.M. Albella, J. Martinez-Duart, *Sol. Cells* 8 (1983) 263.
- [30] A.S. Hovhannisyan, *J. Contemp. Phys.* 43 (2008) 136.
- [31] K. Schmitt, K. Oehse, G. Sulz, C. Hoffman, *Sensors* 8 (2008) 711.
- [32] B. Unal, M.C. Netti, M.A. Hassan, P.J. Ayliffe, M.D.B. Charlton, F. Lahoz, N.M.B. Perney, D.P. Shepard, C.Y. Tai, J.S. Wilkinson, G.J. Parker, *IEEE J. Quantum Electron.* 41 (2005) 1565.
- [33] A.Z. Subramanian, C.J. Oton, D.P. Shepard, J.S. Wilkinson, *IEEE Photonics Technol. Lett.* 22 (2010) 1571.
- [34] A.Z. Subramanian, C.J. Oton, J.S. Wilkinson, R. Greef, *J. Lumin.* 129 (2009) 812.
- [35] K. Bange, C.R. Ottermann, O. Anderson, U. Jeschkowski, M. Laube, R. Feile, *Thin Solid Films* 197 (1991) 279.
- [36] C. Garapon, C. Champeaux, J.dal. Mugnier, *Appl. Surf. Sci.* 96 (1996) 836.
- [37] H.A. Durand, J.H. Brimaud, O. Hellman, H. Shibata, Y. Makita, D. Gesbert, P. Meyrueis, *Appl. Surf. Sci.* 86 (1995) 122.
- [38] E.K. Kim, M.H. Son, S.-K. Min, Y.K. Han, C.H. Wang, S.S. Yom, *J. Appl. Phys.* 79 (1996) 4459.
- [39] R. Rabady, I. Avrutsky, *Appl. Opt.* 44 (2005) 378.
- [40] C. Garapon, C. Champeaux, J. Mugnier, G. Panczer, P. Marchet, A. Catherinot, B. Jacquier, *Appl. Surf. Sci.* 96–98 (1996) 836.
- [41] Z. Jiwei, Y. Tao, Z. Liangying, Y. Xi, *Ceram. Int.* 25 (1999) 667.
- [42] I. Tsyganov, M.F. Maitz, E. Wieser, F. Prokert, E. Richter, A. Rogozin, *Surf. Coat. Technol.* 174–175 (2003) 591.
- [43] K.L. Choy, B.J. Su, *J. Mater. Sci. Lett.* 18 (1999) 943.
- [44] S. Zhang, R. Xiao, *J. Appl. Phys.* 83 (1998) 3842.
- [45] R.J. Gaboriaud, F. Pailloux, P. Guerin, F. Paumier, *J. Phys. D: Appl. Phys.* 33 (2000) 2884.
- [46] A. Kasikov, *Appl. Surf. Sci.* 254 (2008) 3677.
- [47] T.T. Van, J.P. Chang, *Appl. Phys. Lett.* 87 (2005) 011907.
- [48] H. Guo, Y.M. Qiao, *Opt. Mater.* 31 (2009) 583.
- [49] A. Ubaldini, M.M. Carnasciali, *J. Alloys Compd.* 454 (2008) 374.
- [50] A. Polman, *J. Appl. Phys.* 82 (1997) 1.
- [51] B.J.H. Stadler, M. Oliver, *J. Appl. Phys.* 84 (1998) 93.
- [52] R.J. Gaboriaud, F. Paumier, F. Pailloux, P. Guerin, *Mater. Sci. Eng., B* 109 (2004) 34.
- [53] S.J. Pearce, G.J. Parker, M.D.B. Charlton, J.S. Wilkinson, *J. Vac. Sci. Technol., A* 28 (2010) 1388.
- [54] A. Duparre, E. Welsch, H.G. Walther, N. Kaiser, H. Muller, E. Hacker, H. Lauth, J. Meyer, P. Weissbrodt, *Thin Solid Films* 187 (1990) 275.
- [55] P. Gao, L.J. Meng, M.P. dos Santos, V. Teixeira, M. Andritschky, *Vacuum* 56 (2000) 143.
- [56] S. Venkataraj, O. Kappertz, H. Weis, R. Drese, R. Jayavel, M. Wuttig, *J. Appl. Phys.* 92 (2002) 3599.
- [57] K. Koshi, J. Holsa, P. Juliet, *Surf. Coat. Technol.* 120–121 (1999) 303.
- [58] J. Gottmann, A. Husmann, T. Klotzbucher, E.W. Kreutz, *Surf. Coat. Technol.* 100 (1998) 415.
- [59] J.H. Ko, S.H. Kim, S.H. Jee, Y.S. Yoon, D.-J. Kim, *J. Korean Phys. Soc.* 50 (2007) 1843.
- [60] W.C. Liu, D. Wu, A.D. Li, H.Q. Ling, Y.F. Tang, N.B. Ming, *Appl. Surf. Sci.* 191 (2002) 181.
- [61] A. Tamm, M. Kemell, J. Kozlova, T. Sajavaara, M. Tallarida, K. Kukli, V. Sammelselg, M. Ritala, M. Leskela, *J. Electrochem. Soc.* 157 (2010) G193.
- [62] W. Qiu, Y.M. Kang, L.L. Goddard, *Appl. Phys. Lett.* 96 (2010) 141116.
- [63] O. Pons-Y-Moll, J. Perriere, E. Millon, R.M. Defourneau, D. Defourneau, B. Vincent, A. Essahlaoui, A. Boudrioua, W. Seiler, *J. Appl. Phys.* 92 (2002) 4885.
- [64] Y. Zhao, Y. Qian, W. Yu, Z. Chen, *Thin Solid Films* 286 (1996) 45.
- [65] D.L. Rode, V.R. Gaddam, Ji H. Yi, *J. Appl. Phys.* 102 (2007) 024303.
- [66] J.A. Thornton, *J. Vac. Sci. Technol., A* 11 (1974) 666.
- [67] N. Martin, A.M.E. Santo, R. Sanjinés, F. Lévy, *Surf. Coat. Technol.* 138 (2001) 77.
- [68] H.-C. Chen, C.-C. Lee, C.-C. Jaing, M.-H. Shiao, C.-J. Lu, F.-S. Shieu, *Appl. Optics* 45 (1979).
- [69] P. Lobl, M. Huppertz, D. Mergel, *Thin Solid Films* 251 (1994) 72.
- [70] Y.S. Kim, W.H. Kim, *Opt. Mater.* 14 (2000) 229.
- [71] K. Worhoff, J. Bradley, F. Ay, D. Geskus, T.P. Blauwedraat, M. Pollnau, *IEEE J. Quantum Electron.* 45 (2009) 454.
- [72] M.M. Aslan, N.A. Webster, C.L. Byard, M.B. Pereira, C.M. Hayes, R.S. Wiederkehr, and S.B. Mendes, *Thin Solid Films* 518 (2010) 4935.
- [73] M.F. Al-Kuhaili, *Thin Solid Films* 426 (2003) 178.
- [74] J.J. Chambers, B.W. Busch, W.H. Schulte, T. Gustafsson, E. Garfunkel, S. Wang, D.M. Maher, T.M. Klein, G.N. Parsons, *Appl. Surf. Sci.* 181 (2001) 78.
- [75] P. de Rouffignac, J.-S. Park, R.G. Gordon, *Chem. Mater.* 17 (2005) 4808.
- [76] T. Tsutsumi, *Jpn. J. Appl. Phys.* 9 (1970) 735.
- [77] M.-S. Kim, Y.-D. Ko, J.-H. Hong, M.-C. Jeong, J.-M. Myoung, I. Yun, *Appl. Surf. Sci.* 227 (2004) 387.
- [78] E.K. Evangelou, C. Wiemer, M. Fanciulli, M. Sethu, W. Cranton, *J. Appl. Phys.* 94 (2002) 318.